The University of Chicago
Center for Integrating Statistical and Environmental Science
www.stat.uchicago.edu/~cises

Chicago, Illinois USA

TECHNICAL REPORT NO. 38

TRACKING SUSPENDED SEDIMENT MOTION IN LAKE MICHIGAN BY COMBINING SATELLITE IMAGES WITH A NUMERICAL MODEL

Jonathan Stroud, Barry Lesht, David Schwab, Dmitry Beletsky, Michael L. Stein

August 2006

Although the research described in this article has been funded wholly or in part by the United States Environmental Protection Agency through STAR Cooperative Agreement #R-82940201 to The University of Chicago, it has not been subjected to the Agency's required peer and policy review and therefore does not necessarily reflect the views of the Agency, and no official endorsement should be inferred.

Tracking Suspended Sediment Motion in Lake Michigan by Combining Satellite Images with a Numerical Model

Jonathan Stroud*, Barry Lesht†, David Schwab‡, Dmitry Beletsky§, Michael Stein¶

August 4, 2006

Abstract

Because satellite observations are synoptic, collected frequently, and highly resolved on geophysical scales, they can be a valuable source of information for development and application of numerical models. Data derived from satellite sensors may be used in model evaluation studies, as well as for operational and prognostic updating of both model state and forcing variables. Although satellite data are used routinely with many types of operational atmospheric models, little work has been done to integrate satellite data with models of aquatic systems. In this paper we develop and examine schemes for combining daily images obtained by the Sea-viewing Wide Field Spectrometer (SeaWiFS) with a two-dimensional sediment transport model representing southern Lake Michigan. We perform a forecasting study focused on a two-month period in spring 1998 when a large storm caused substantial amounts of sediment resuspension and horizontal sediment transport in the lake. We find that data assimilation schemes improve forecast root-mean-square-error (RMSE) by 40% over purely model-based approaches and by 20% over purely data-based approaches.

*Department of Statistics, University of Pennsylvania (E-mail: stroud@wharton.upenn.edu)
†Applied Science and Technology Directorate, Argonne National Laboratory (E-mail: bmlesht@anl.gov)
‡NOAA/GLERL, Ann Arbor, MI (E-mail: david.schwab@noaa.gov)
§CILER, SNRE, University of Michigan (E-mail: dima.beletsky@noaa.gov)
¶Department of Statistics, University of Chicago (E-mail: stein@galton.uchicago.edu)

1 Introduction

Recent improvements in computer performance have led to increases in the complexity of geophysical models. Similarly, improvements in data visualization methods have led to increased emphasis on models with detailed spatial and temporal resolutions, the output of which can be presented in dramatic graphical form. Both developments in modeling have highlighted the importance of obtaining field data appropriate for evaluating and improving complex, highly resolved models. This is true particularly in the Great Lakes, because numerical models have been among the primary tools employed for understanding and assessing these systems since the 1970s, when phosphorus-induced eutrophication was the primary concern of lake managers.

Current generation models are based on grid scales of O(1)-km and run on hourly or sub-hourly time steps, hence traditional ship-based surveys cannot collect data with either the spatial or temporal density the models need for their support. High-frequency data can be collected with instruments mounted on fixed moorings, but like ship-based surveys, these are costly unless the spatial domain of interest is small. Satellite remote sensing, which can provide information that is highly resolved in both space and time, is a promising source of data that are better matched to the models' spatial and temporal scales and that should prove most valuable for model evaluation and development.

Of course, satellite methods are neither problem-free nor without serious challenges of interpretation. Some of these difficulties can be overcome by limiting the application of the observations to variables that are most directly related to the satellite measurements (e.g., surface temperature) and/or by taking advantage of temporal and spatial compositing to extract meaningful signals from inherently noisy data. Indeed, a rich body of literature has shown that valuable data can be obtained from satellite imagery, especially for studies of regional-scale and seasonal processes (Brock and McClain, 1992; Uddstrom and Oien, 1999; Behrenfeld et al., 2001).

Satellite observations can also be used to understand shorter-term and localized phenomena. For example, we used a three-month time series of satellite images obtained from the Sea-viewing Wide Field Spectrometer (SeaWiFS) sensor to study a rapidly developing phytoplankton bloom in southern Lake Michigan (Lesht et al., 2002). Other researchers (Hughes et al., 1998; Kostinoy et al., 2004) used high-frequency imagery to study transient events in the open ocean. Relatively little work, however, has been directed toward integrating high-frequency, high-resolution imagery with high-resolution models of aquatic processes. Such integration should be useful both as a quantitative measure of the models' performance and for providing operational models with data for near-real-time assimilation (Schwab and Bedford, 1994).

The purpose of this paper is to report on our exploration of methods for combining

satellite imagery with a high-resolution numerical model. More specifically, we discuss here our integration of SeaWiFS data with a model originally developed for simulating sediment transport in Lake Michigan. Understanding and predicting the movement of suspended sediment is important in the Great Lakes, because many of the contaminants of concern in these waters are associated with fine particles, and all of the major nutrient cycles (carbon, nitrogen, phosphorus, and silicon) include significant particulate phases. The complex biogeochemical models (Chen et al., 2004) being developed to assist in management of the lakes reflect this fact and depend critically on accurate representation of sediment transport processes. Even simple biogeochemical models of the Great Lakes have been shown to be most sensitive to their parameterizations of sediment transport (Chapra, 1977; Lesht et al., 1991).

Much work has been devoted to Great Lakes sediment modeling. Because data continuity has been valued more than possibly fragmented information about spatial and temporal patterns, and because time series are easier to manage than are the large three-dimensional (3-D) data sets provided by satellites, sediment model validation studies have used time series observations made at single points rather than satellite imagery. On the other hand, suspended sediments are highly reflective, and they are easily detectable in visible-wavelength satellite images. Thus, the application of satellite data to studies of sediment transport in marine and aquatic systems remains an active area of research.

The first well-known exploration of satellite imagery of Lake Michigan highlighted intriguing spatial patterns indicating complex current structures (Mortimer, 1988) but did not attempt quantitative analyses. Other early studies in marine systems used very small sets of data for limited purposes, probably because the requirements for dealing with the satellite data exceeded the available computing capacity. For example, Puls et al. (1994) compared three cloud-free Coastal Zone Color Scanner images of the North Sea with a model calculation and concluded simply that their model did not successfully reproduce the observed sediment distributions. As computer memory and storage technology advanced, studies became more sophisticated and quantitative, but they still were often based on small sets of satellite images and limited model calculations (Gerritsen et al., 2001; Ransibrahmanakul and Stumpf, 2002; Ouillon et al., 2004; Pleskachevsky et al., 2005). None of these studies used satellite data either to evaluate the performance of the models as they progressed in time or to examine the effects of incorporating past data into the model to improve forecasts. These two applications are our primary focus here.

In Section 2 we describe the data and the numerical model, and in Section 3 we discuss several concepts of forecasting and our approaches to image-model integration. Our results are described in Section 4. In Section 5 we discuss the performance of the forecasts in some detail and illustrate how the relationships between the forecasts and observed fields

provide insight valuable for improving the model and for understanding the limitations of the data. We conclude that real-time and retrospective modeling of sediment transport can be enhanced substantially by incorporating satellite imagery and that the data provided by the satellites can be important both for constraining model results and for assessing the choice of model parameter values.

2 Satellite Data and Model

2.1 Satellite Images

We concentrated our analysis on a 60-day time period spanning March-April 1998, when a major sediment resuspension event occurred in southern Lake Michigan. An intensive data collection effort, known as the Episodic Events Great Lakes Experiment (EEGLE; http://www.glerl.noaa.gov/eegle/), that also began at this time is the source of the in situ data we used in this work. The resuspension event has been described in several papers resulting from the EEGLE project (Schwab et al., 2000; Eadie et al., 2002). For our purposes, the points of importance are that resuspension events like the one in 1998 appear to have significant influences on lake processes, the events are easily visible in satellite images, and considerable effort has been devoted to developing models that simulate the effects of the events on the lake's biogeochemical function (Chen et al., 2004).

We used imagery from SeaWiFS, obtained from the Ocean Color archive of the National Aeronautics and Space Administration (NASA) Goddard Space Flight Center (http://oceancolor.gsfc.nasa.gov), in this study. We limited the data selection to overpasses between 12:40 and 14:40 local time and converted the Level 1 images obtained from the archive to Level 2 products by using NASA's SeaDAS software (Baith et al., 2001). The output products used in our analysis included remote sensing reflectance (R_{RS}) in the eight SeaWiFS bands (six in the visible and two in the near infrared), as well as several auxiliary diagnostic variables. Our processing included an atmospheric correction (Gordon and Wang, 1994), a modified cloud detection and masking value (albedo at 865 nm $\geq$ 1.25%), and mapping onto a 2-km grid that was coincident with the model grid described below. For our basic analysis we further screened the images to eliminate those having fewer than 3500 cloud-free pixels among the 7347 pixels covering the southern basin. A total of 20 images, described in Table 1, passed this screening.

2.2 In Situ Data

Using satellite data to retrieve the values of geophysical variables can be an involved process. The radiances received at the satellite must be corrected for the confounding effects of the atmosphere and a functional relationship must be determined between the corrected

radiances and the variable of interest. Very often such relationships, or retrieval algorithms, are developed empirically. Many so-called semi-empirical algorithms have been proposed for retrieving suspended sediment concentration or total suspended material (TSM) from satellite observations from a variety of sensors and bands (Mitchelson-Jacob, 1999). Several groups (Myint and Walker, 2002; Binding et al., 2003, 2005; Budd and Warrington, 2004; Chen et al., 2004; Warrick et al., 2004, and others) have published suspended sediment algorithms specific for SeaWiFS. Using data from coastal Louisiana, Myint and Walker (2002) explored several statistical relationships between suspended sediment concentration and radiance in single SeaWiFS bands (555 nm and 670 nm) and determined that a quadratic model based on the 670-nm band fit the data best. In their study of suspended sediments in the Irish Sea, Binding et al. (2003) used similar statistical methods and also adopted a quadratic model that related reflectance (rather than radiance) at 670 nm to suspended sediment concentration. Similar work in the Great Lakes has been very limited. Budd and Warrington (2004) used SeaWiFS observations to derive linear relationships between suspended sediment and reflectance at 555 nm for both Lake Michigan and Lake Superior. Chen et al. (2004) used much of the same data set to derive two log-linear relationships, one for each year of their study, predicting suspended sediment concentration as an exponential function of reflectance at 555 nm.

Because the parameter estimates by Chen et al. (2004) varied substantially across their two study years, and because their fitted functions do not reproduce the reflectance when TSM concentrations are high, we used in situ data collected during EEGLE to develop a new calibration function relating suspended sediment concentration to remote sensing reflectance. The locations of these EEGLE samples, along with the bathymetry of the southern basin, are shown in Figure 1 (left). In total, EEGLE investigators made 65 near-surface TSM measurements in March and April of 1998 and 1999. After a careful screening, we removed three outliers and matched the remaining 62 measurements by location and collection time with the nearest pixel of our SeaWiFS images (Figure 1, right). Twenty-six of the samples, summarized in Table 2, were collected in 1998 during our study period and are used in our forecast evaluation.

We tested several relationships between the SeaWiFS observations and TSM measurements, including those described above, and found that the function

$$R_{RS}(555) = .0027 + .0537 \log(1 + .4739\, TSM), \tag{1}$$

plotted in Figure 1, best represented the data. This function is linear at small values of TSM and logarithmic at large values. We also use the inverse function,

$$TSM = 2.11 \left\{ \exp[18.62\, R_{RS}(555) - .05] - 1 \right\}, \tag{2}$$

in the data assimilation schemes described Section 3.

2.3 Sediment Transport Model

Sediment transport models generally are designed to simulate the time-varying distribution of particles in the water column and sediment bed as they respond to gravitational and hydrodynamic forces. These models vary in complexity from those that yield a time series of suspended sediment concentration at a single point (Hawley and Lesht, 1992) to those that calculate the vertical profiles of several size classes of sediments both in the water column and the bed as they change in both space and time (Lee et al., 2005). The model we use here, which simulates the temporal and spatial evolution of the depth-averaged concentration of a single sediment class as the lake responds to wind forcing, is of intermediate complexity.

The hydrodynamic models used in this study include a circulation model (Beletsky and Schwab, 2001; Beletsky et al., 2003) that is based on the 3-D Princeton Ocean Model (POM) and a surface wave model (Schwab et al., 1984). Bottom horizontal shear stress is calculated as a linear function of independent stresses resulting from the full 3-D POM and from the wave model. In our application, the horizontal flows are calculated by vertically integrating the results of the 3-D model.

Several studies (Lesht and Hawley, 1987; Lesht, 1989) have shown that wave stress dominates the current stress in the Great Lakes and that the primary role of the wind-forced currents is advection of material resuspended from the bottom by the wave stress (Schwab and Beletsky, 2002). Sediment resuspension is parameterized in the model in terms of excess bottom shear stress, where the threshold or critical stress is given, as are the parameters representing the sediment settling rate and resuspension rate. The model also includes the dynamics of the sediment bed, representing the quantity of sediment available for resuspension in terms of bed thickness at every grid cell. The model initial conditions and parameter values are listed in Table 3.

Using this general framework, we write

$$(d+\eta)\frac{\partial c}{\partial t} = -u\frac{\partial c}{\partial x} - v\frac{\partial c}{\partial y} + s, \tag{3}$$

$$\frac{\partial b}{\partial t} = -\frac{s}{\rho}, \tag{4}$$

where $c \equiv c(x,y,t)$ and $b \equiv b(x,y,t)$ denote the vertically-averaged sediment concentration and sediment bed thickness at location (x,y) and time t; $d \equiv d(x,y)$ denotes the local water depth; $\eta \equiv \eta(x,y,t)$ the free surface fluctuation; $u \equiv u(x,y,t)$, and $v \equiv v(x,y,t)$ are the water velocities; $s \equiv s(x,y,t)$ is the vertical flux, which incorporates resuspension and settling; and ρ is the sediment density (Krone, 1962; Partheniades, 1962).

We assume bed-limited resuspension, so that $s = \min(s^*, \kappa\, b)$, where $\kappa = 250$ is the density-based factor relating the bed thickness to the sediment mass and s^* is the vertical

flux for a bed of unlimited thickness, defined as

$$s^* = -w_s c \; + \; \epsilon \left(\frac{\tau}{\tau_c} - 1 \right) \mathbf{1}(\tau \geq \tau_c). \tag{5}$$

Here $\tau = \tau(x, y, t)$ is the bottom shear stress, w_s is the settling velocity, τ_c is the critical bottom shear stress, ϵ is the resuspension rate, and $\mathbf{1}(\cdot)$ is an indicator function that takes the value one when the argument is true and zero otherwise. We implemented this model on a 2-km grid representing Lake Michigan. The grid consists of 131 columns by 251 rows, and a total of 14,458 water cells.

3 Methods

We consider the following forecasting problem: Given an initial condition, expressed here as the spatial distribution of TSM on the 2-km grid, how do we best predict the evolution of the R_{RS} field in time? Because we are concerned with the relative accuracy of our forecasts, we present most of our results in terms of the transformed variable log R_{RS}, and we emphasize relative rather than absolute errors. We conducted similar analyses on several scales of the response variable, including TSM and R_{RS}, and determined that this transformation does not materially affect the results (see Table 4).

Of course, forecasting methods vary considerably in complexity. Although we assumed that the best forecasting technique would involve application of a physically based numerical model driven by specified time series observations of external forcing mechanisms, we also considered forecast methods that do not include lake dynamics. Our ultimate goal, again, is to determine the extent to which concurrent observations of the state of the system, provided by satellite measurements, can improve the accuracy of the resultant forecasts. By using the satellite images for comparison with the forecasts, we can both explore and quantify the attributes of the various forecast methods. Note that we distinguish here between forecasting, in which we use the model and past data to predict a future state of the system, and smoothing, in which we might look ahead in time and retrospectively adjust the model trajectory to match a known future state.

3.1 Climatology

The simplest non-trivial (e.g., spatially invariant constant value) forecast one can make is that the TSM distribution in the lake has spatial structure but does not evolve in time. To establish a base case against which to compare the results of more complex forecasting methods, we used data not included in our analysis to estimate the average lake log R_{RS} field during March-April 1998. We defined the "climatologic" mean field as the average of the log R_{RS} at each pixel measured by satellite during March-April 1999-2000 (the two

years following our study year). This field then was used as the forecast field at each subsequent image time. Thus, the climatological forecast error represents the deviation of the observations from the climatologic values.

3.2 Persistence

The next level of forecast complexity incorporates the available satellite data to update the climatologic mean. Like the climatological case, the forecast does not account for either lake or sediment dynamics; the state variable value at every pixel remains fixed until another observation is available. In this scheme, after initializing the system with the climatologic values, we set the forecast value at each pixel equal to the most recent cloud-free satellite observation at that location. The forecast errors in this case represent the differences between sequential observations. Thus, errors may be interpreted in terms of the "persistence" of the state variable in time.

3.3 Pure Numerical Model

We also calculated forecasts based entirely on the sediment transport model without data updating. This scheme provides a base case against which to compare the forecasting schemes that incorporate both the model and data. For the pure model forecasts, we ran the full model forward from the fixed initial conditions given in Table 3, forcing it with the meteorological wind fields interpolated from observations (see Beletsky et al., 2003), to simulate the entire modeling period. At each image time point, the forecast errors are based on the differences between the observed satellite data fields and the modeled fields at that time.

3.4 Modeling with Data Assimilation

Each of the forecasting methods described above relies on either the physical model or the satellite data, but not both. By combining these two sources of information, we might hope for a substantial reduction in forecast errors, though this is not necessarily the case. If both the model and data were badly in error, combining them would merely confound the problems. Adding bad data to a good model would diminish the value of the model; similarly, using a bad model with good data still would yield unreliable forecasts. Many methods have been developed for combining models and data, though often without recognition of the implicit assumption that both model and data provide some reasonable representation of the system of interest. Generally known as data assimilation (Kalnay, 2003), the methods are intended to capture the best of both approaches, though implementation varies considerably from application to application.

Our general assimilation scheme incorporates the data sequentially into the model forecasts in a conceptually simple manner. In all cases, we initialize the assimilation by setting the model TSM and sediment bed thickness fields to the constant values given in Table 3. We then run the sediment transport model forward with the prescribed meteorological forcing until the first image time (282 hours after initialization). We use Eqs. (1) and (2) to convert between TSM and log R_{RS}. Subsequently, we repeat the following steps for each image:

1. Convert the modeled TSM field to log R_{RS}.
2. Compute the forecast error as the difference between the image and model values.
3. Update the modeled log R_{RS} field by using the assimilation scheme being tested, and convert the model field back to TSM.
4. Run the model forward to the next image time.

The algorithm above provides a sequence of one-image-ahead forecasts. The one-ahead error is calculated from the differences between each image and the corresponding forecast. We also determined k-image-ahead forecast errors by running the model with updates to image i and then running ahead without updates to the end of the T-image series, calculating the forecast error at every image $i+k$ for $1 \leq k \leq T-i$. Because the results of the two methods did not differ substantially, we discuss only the one-image-ahead results here.

Note that the number of pixels included in the forecast error calculation (Step 2) depends on the completeness of the image and that our image screening guaranteed that at least 3500 pixels were used. Also note that to minimize the potential effect of model spin-up time on the comparison among forecast methods we did not use the first image (hour 282) in the error analysis. Because the satellite images do not directly inform us about changes in the sediment bed, we do not update the sediment bed thickness at Step 3. Long-term mass conservation is not required in the model, however, because in reality new sediment is introduced into the lake by shoreline erosion and direct deposition during the course of the year. Because the model includes gravitational settling, some of the changes in the modeled suspended sediment mass introduced by the updating eventually result in changes in the bed thickness.

We focus here on the results obtained from two update schemes: direct insertion and kriging. Certainly, many other assimilation schemes are in common use (see Kalnay, 2003), but these two depend only on past data and are appropriate in the pure forecasting mode that we are testing.

3.4.1 Direct Insertion

Conceptually, the direct insertion method is easy to describe: We "insert" the satellite data values into the numerical model whenever observations occur. In other words, at a given image time, the forecast values at the cloud-free locations are replaced with the corresponding satellite values, while the remaining forecast values are left unchanged. The advantage of this approach is its conceptual and computational simplicity. During the update, the state variable at any location takes the value of the observation made at the same location. Thus, the computational cost is proportional to the number of observations. On the other hand, the approach can lead to artificial discontinuities in the updated field when the satellite images are incomplete and the time between updates is long. As we will see in Section 5, this may occur along the boundaries of cloud-covered areas or where a forecast-data mismatch occurs. Note that the persistence forecasting procedure (Section 3.2) is equivalent to the direct insertion method without the lake or sediment dynamics.

3.4.2 Kriging

To reduce or avoid spatial discontinuities in the results, it may be desirable to replace the model forecasts with completely updated fields rather than with the partially updated fields that may be used in direct insertion. One method of producing a completely updated field is to interpolate the observations to estimate new values at every grid cell. Kriging-based approaches (see, for example, Cressie, 1993) provide a method for spatial interpolation that is optimal if one can properly specify the covariance among the observations and the forecasts. The covariance function may be based on analysis of the data fields or may be pre-specified, depending on the application. Given a set of data and a covariance function, the so-called kriged values are the best linear, unbiased estimates of the variable values at all locations.

At each image time, we represent the observed data by

$$\mathbf{y}^o = \mathbf{H}\mathbf{y}^f + \mathbf{e}, \tag{6}$$

where $\mathbf{y}^o$ is the $m \times 1$ satellite data vector, $\mathbf{y}^f$ is the $n \times 1$ model forecast vector, $\mathbf{e}$ is the $m \times 1$ forecast error vector (all expressed in units of log R_{RS}), and $\mathbf{H}$ is an $m \times n$ matrix with jth row given by $\mathbf{h}_j = (0, \ldots, 0, 1, 0, \ldots, 0)$, where the position of the 1 indicates which component in the forecast vector corresponds to the jth observation.

Under the kriging model in Eq. (6), the error $\mathbf{e}$ subsumes all possible sources of uncertainty in the forecasts and the observations, including errors in the numerical model, misspecification of the calibration function, errors in the atmospheric correction algorithm, and satellite sensor and geographic displacement errors. The kriging model is intended to

account for any spatially correlated forecast errors that result from the unknown uncertainties expressed by $\mathbf{e}$. For our analysis, we assume the error vector $\mathbf{e}$ is random with mean $\boldsymbol{\mu}$ and covariance defined by the function $cov[e(\mathbf{s}), e(\mathbf{s}')] = C(d;\theta)$, where $e(\mathbf{s})$ and $e(\mathbf{s}')$ are the errors at spatial locations $\mathbf{s}$ and $\mathbf{s}'$, $d = ||\mathbf{s} - \mathbf{s}'||$ is Euclidean distance, and θ is a set of covariance parameters.

For the analysis in Section 4, we assume that the errors have mean $\boldsymbol{\mu} = \mathbf{0}$ (i.e., the forecasts are unbiased estimates of the observations) and the covariance function

$$C(d;\theta) \;=\; \sigma^2 \exp(-d/\lambda)\, k_r(d), \tag{7}$$

where $\theta = (\sigma^2, \lambda, r)$ is the parameter vector, σ^2 is the theoretical variance of the forecast errors, λ is the range or distance scale typical of the covariance between points, and $k_r(d)$ is the correlation function $k_r(d) \in [0,1]$ proposed by Gaspari and Cohn (1999, Eq. 4.10), which equals zero for distances beyond r. This correlation function eliminates very small values of the covariance function for point combinations where d is large. Typically, we choose r to be small, so that the intra-site covariance is set equal to zero for most pairs of locations. As we shall discuss further, this reduces the computational cost considerably. The covariance function in Eq. (7) was chosen after experimenting with a number of other functions, including various members of the Matèrn family (see Stein, 1999), various non-stationary and anisotropic covariance functions, and those that included a measurement error term. However, using these other functions did not substantially improve the overall forecast performance in terms of log R_{RS}.

Given our model for the forecast errors, the kriging update step proceeds as follows. Let $\boldsymbol{\Sigma}$ denote the $n \times n$ covariance matrix for the errors, with elements given by $\Sigma_{ij} = C(d_{ij};\theta)$, where $d_{ij} = ||\mathbf{s}_i - \mathbf{s}_j||$ are the distances between the model gridpoints. The updated field $\mathbf{y}^u$ is then given by the formula

$$\mathbf{y}^u \;=\; \mathbf{y}^f + \mathbf{K}\mathbf{e}, \tag{8}$$

where $\mathbf{K} = \boldsymbol{\Sigma}\mathbf{H}'(\mathbf{H}\boldsymbol{\Sigma}\mathbf{H}')^{-1}$ is the $n \times m$ matrix of kriging weights. Direct calculation of Eq. (8) is computationally demanding, as it requires solving a system of order m, which is quite large in our application ($m > 3500$). To alleviate this problem, we perform the update with an efficient conjugate gradient algorithm (see Appendix) that exploits the gridded nature of the data and the assumption of a sparse covariance matrix (since r is chosen to be small). The result of Eq. (8) is a complete field, $\mathbf{y}^u$, that matches the data $\mathbf{y}^o$ at the observed locations and is continuous over the entire domain. Note, however, that if we assume that the forecast errors are spatially uncorrelated ($\lambda \approx 0$), then the updated field will match the forecasts, $\mathbf{y}^f$, at the unobserved locations; in this case the results are equivalent to those produced by the direct insertion approach.

4 Results

We applied the forecasting methods described above to SeaWiFS data collected in March-April 1998. As noted above, this time period included a major resuspension event in southern Lake Michigan. Strong (20 m/s) north winds blowing along the long axis of the lake for several days in early March 1998 generated waves at the south end of the lake that exceeded 6 m in height. When the storm passed and the sky cleared on March 12, satellite images showed a region of high reflectance, interpreted as newly resuspended and eroded sediments, extending along the entire southern coastline of the lake (approximately 300 km). Subsequent satellite images collected over the next several weeks showed both along- and cross-shore transport of the suspended sediment, corresponding to the general counterclockwise circulation pattern in this part of Lake Michigan (Beletsky and Schwab, 2001). Other smaller events later in March and in early April added to the sediment burden, especially near the shore. By the middle of April, the water column was almost clear of suspended sediment, and the minimum R_{RS} values were at or below 1% for the rest of the month, especially in the offshore area.

In the ideal case, the forecasts would perfectly match the data at each point in space and time. In practice, of course, we must consider the effects of systematic errors in both the model and data, as well as random errors that might result from factors like poor or inconsistent registration of the satellite images or misspecification of the TSM/R_{RS} calibration function. We attempted to account for the data and forecast uncertainty by calculating the errors associated with various linear combinations of the data (*e.g.,* areal averages of blocks of neighboring pixels and spatial differences or gradients in different directions). We found that most of these were uninformative relative to the pixel-by-pixel errors. When broken out by region (Figure 1), however, the east-west gradients, calculated for each pixel pair by subtracting the west pixel value from the adjacent east pixel value, showed evidence of model bias, which is discussed in Section 5.

We characterized the results of the forecasting methods statistically in terms of bias and root-mean-squared error (RMSE). Let Y_{tj} denote the function of the satellite data (i.e., pixel value, block average, gradient) at time t and location j, $\hat{Y}_{tj}$ the predicted value, and N the number of observations used to compute the statistic. We then defined

$$\text{Bias} \;=\; \frac{1}{N}\sum_{t,j}(Y_{tj}-\hat{Y}_{tj}) \quad \text{and} \quad \text{RMSE} \;=\; \sqrt{\frac{1}{N}\sum_{t,j}(Y_{tj}-\hat{Y}_{tj})^2}.$$

Table 4 summarizes these statistics for the one-image-ahead forecasts.

4.1 Climatology

The error statistics listed in Table 4 show that the climatological forecast performs poorly. The RMSE across the 19 images is only slightly smaller than the overall standard deviation of the observations for log R_{RS}, and it is larger than the RMSE values for the other forecast methods tested. When compared with the 26 in situ samples (Table 2), the climatological forecasts are more variable, and their mean is 60% below the observed mean. The problem with the climatological forecast is illustrated in Figure 2, which shows the results obtained by using the persistence method (presented in more detail below). The top row of the figure depicts the retrieved satellite data from the first six images in our data series. The middle row shows the forecast fields at each image time and the bottom row shows the differences between the two. Because the persistence method does not include lake or sediment dynamics, the first forecast shown (middle row, column 1) is simply the climatological mean determined from the 1999-2000 data. Even though the climatological field shows increased sediment concentrations near the coasts in the southern basin due to spring resuspension events that occurred in 1999 and 2000, the sediment concentrations are much smaller than those observed in 1998. As a result, the errors in the first forecast (bottom row, column 1) are substantial. Because the climatological forecast is constant in time, the same forecast field (middle row, column 1) is used for every one of the subsequent images. Only when the high sediment concentrations associated with the March 1998 event are reduced by settling and advection do the errors associated with the climatological forecast fall to levels near zero.

4.2 Persistence

The persistence method, which incorporates the satellite data without lake or sediment dynamics, substantially reduces the forecast errors. The RMSE value for log R_{RS} is approximately 40% lower for forecasts using persistence than for the climatological forecasts (Table 4). With respect to the in situ samples, the persistence method has the smallest bias of the methods considered, but a relatively large RMSE for TSM. The persistence forecasts are updated by using the last set of satellite observations. As Figure 2 shows, the updated forecasts (e.g., middle row, column 2) are calculated by replacing the prior forecast values (middle row, column 1) with the available data (top row, column 1). Not surprisingly, the magnitude of the errors depends on the time interval between the observations and the completeness of the data set used for updating. Examination of the error images (bottom row) shows, for example, that because much of the east coast of the lake was cloud covered at hour 282, the forecast for hour 283 (next available image) assigned the climatological values (middle row, column 1) to these pixels. Because fewer pixels along the east coast were cloud covered at hour 283 and also had log R_{RS} values higher than the corresponding

forecast values, the errors along the east coast are large and positive (row 3, column 2).

The importance of including lake dynamics in the forecasts is clearly shown by the persistence forecast errors at hour 379 in Figure 2 (bottom row, column 3). In the 96 hours between the second and third observations, the highly reflective area on the eastern side of the lake has both changed shape and moved north. Because the persistence forecast does not include dynamics, it cannot represent this movement, and the error image shows a positive error at the new location of the reflective area and a negative error at its previous location. We note that such negatively correlated errors may cancel out when images are averaged over time, which suggests a possible limitation of model-satellite comparisons that are based solely on the long-term statistical distributions of state variables. We avoid this limitation with the image-by-image analysis reported here.

4.3 Pure Numerical Model

Figure 3 shows the forecast results obtained by using the pure model. Although the model was initialized to spatially constant conditions and is based on the spatially uniform and nominal (though realistic) sediment transport parameters listed in Table 3, it reasonably reproduces the general sediment concentration patterns we see in the observations. In particular, the pure model does very well at representing the long, narrow band of sediment running up the east coast and also suggests the westward offshore transport of sediment seen in the images at hours 522 and 546.

This apparent qualitative success is not reflected in the error statistics (Table 4), however. Though it performed better than the climatological forecast, the overall errors associated with the pure model forecast are positively biased and have substantially larger RMSE, on all the response scales, than those for the persistence forecast. Much of the error results from the tendency of the pure model to predict wider bands of suspended sediment along the coasts, as well as its understandable failure to simulate the large localized area of high reflectance that appears in the first image and dominates many of the subsequent scenes. The fact that the pure model tends to spread the sediment band beyond the limits suggested by the data also is reflected in the in situ sample statistics; the high bias results from the prediction of lower values than are observed, and the lower RMSE indicates that the forecast errors are smaller than those for the climatology and persistence forecasts. Some of these problems might be alleviated by incorporating a more complex sediment resuspension model or by improvements in the hydrodynamic circulation model.

4.4 Assimilation - Direct Insertion and Kriging

The primary difference between the two assimilation methods used in this study is that kriging allows us to update the entire field at each image time, rather than limiting the

update to the possibly discontinuous set of available pixels used in direct insertion. As noted above, the two methods are equivalent when the range parameter (λ) in the covariance model, Eq. (7), equals zero. Although the two methods differ conceptually, their forecast error statistics presented in Table 4 for the two methods are very similar and we discuss them together. Both reduce the RMSE in log R_{RS} by approximately 50% relative to climatology and approximately 40% when compared to the pure model.

One of the goals of data assimilation is to adjust the model forecasts to agree better with new observations and provide more accurate predictions going forward. We would expect, for example, that the model's tendency to predict wider sediment bands than are observed along the coasts would be mitigated when the forecasts are adjusted to reflect the narrower features typical of the data. Similarly, the problem associated with the model's failure to simulate the localized offshore area of high sediment concentration that appeared on March 12 would be resolved in the subsequent forecasts by the insertion of the March 12 observations during the update step.

The additional step (analysis of the image field being used for update) required for the kriging method is illustrated in Figure 4. Rather than update the forecasts (second row) with the data (top row) at only those pixels for which we have data, as would be the case for direct insertion, under the kriging method we first use Eqs. (6)-(8) to create an analyzed field (third row). The analyzed field is then run forward in time by using the numerical model to create the forecast for the next image (e.g., row 2, column 3, is the forecast based on the updated field shown in row 3, column 2). Note that since our choice of covariance model assumes no measurement error, the direct insertion and kriging updates are the same at pixels for which we have observations. This point is important for understanding why the direct insertion and kriging results are so similar for these data.

5 Discussion

One goal of our analysis was to use the time series of high-resolution observations provided by the satellite to validate the performance of the model. This type of model-data comparison is useful for gaining insight into how well the important physical processes are represented in the model, as well as for model "calibration" or "tuning" and for parameter sensitivity studies. One way to examine the model performance is to isolate the processes represented in the model and determine how they influence the model's success in reproducing the observations. Table 5 shows the results of such an experiment, in which we used direct insertion assimilation to test each of the eight possible combinations of the three model components. The results for the persistence forecast, which is equivalent to direct insertion assimilation without the physical model, are shown for comparison.

Adding the resuspension process alone slightly reduces the variability of the forecast er-

rors but increases the error bias. The higher bias (data minus forecast) is due to the addition of sediment to the water column by the resuspension process without a compensating loss mechanism. When settling is included in the model, the bias is reduced to near zero, and the variability of the errors is reduced further, suggesting that the settling and resuspension parameter values listed in Table 3 are within a reasonable range. The converse situation, when settling is added alone, is highly biased but in the opposite direction. The positive bias reflects the steady loss of material from the water column by settling between update steps. As would be expected, this bias, though still positive, is reduced substantially when advection is added to the settling. The error variability, however, is not much different from that for the case when settling and resuspension are included without advection.

The error variability is reduced substantially when advection is combined with resuspension, indicating the dominant role that local resuspension plays in accounting for the variability in the observations. The large bias, of course, is again the result of adding material without providing for a counterbalancing loss mechanism. Both the bias and RMSE are reduced to their final values when settling is added in the complete model.

We could, in principle, use the bias and RMSE calculations to adjust the sediment model parameters to some set of optimal values. Indeed, we experimented with different sediment bed thicknesses, settling velocity, and resuspension rate values before choosing the set listed in Table 3. To be most useful, however, we also would have had to include a spatial variation in all of these parameters, something we were not prepared to pursue in this study. Our aim was to explore assimilation methods rather than to perform a model calibration exercise (Lee et al., 2005), so adding spatial variability to the parameter values remains a problem for future work.

Analysis based on the whole-basin results allows us to assess the overall performance of the model. Others have commented on the the steep gradient in reflectance associated with the edge of the near-shore resuspension feature, which generally is about 10 km wide (Eadie et al., 1996; Rao et al., 2002). Therefore, evaluation of the model's ability to reproduce this feature is also of interest. We find that the pure model tends to predict wider ($\sim$25 km) near-shore zones of high reflectance and smaller gradients than are seen in the satellite data. To examine this further, we used the differences between adjacent pixels in the east-west direction to estimate the horizontal gradients in the forecast and observed fields and to quantify the ability of the different forecast methods to reproduce the observed gradients (Table 6). Because we expect much more horizontal homogeneity (small gradients) in the offshore areas of the lake and gradients of opposite sign on the west and east coasts, we divided the analysis into three spatial regions (shown in Figure 1), in which the coastal areas were defined as including all pixels with depths shallower than 75 m.

Of the forecasting methods, the two assimilation techniques provide the best gradient

forecasts overall, with bias improvements over the pure model of approximately 70%, 65%, and 95% for the west, offshore, and east regions, respectively. The climatology gradient forecast was quite good, particularly in the west and offshore areas. This success is explained by recalling that the climatology forecast (see middle row, column 1, of Figure 2) is based on the average of all satellite observations made during March and April of 1999 and 2000. Because the nearshore sediment resuspension events are more or less annual phenomena, the general features of these events will be reflected in the climatology. Two of the general features captured by the climatology, the relative homogeneity of the offshore water and the steep gradients, are exactly those we would expect to be reproduced by an accurate model. The dynamics of circulation and sediment transport in Lake Michigan's southern basin display less annual variability along the western shore than along the eastern shore, where northward and southward flowing currents converge (Beletsky and Schwab, 2001). This increased variability accounts for the larger errors in the east region.

Higher bias values indicate that the observed gradients are larger than the modeled ones. This is illustrated in Figure 5, which shows the forecast results and observations for three transects along the southern basin. Because R_{RS} increases near the shore and the gradients are defined as east minus west, the sign of the bias is negative on the west shore and positive on the east. Larger bias values indicate "flatter" forecasts relative to the observations. This result implies that the pure model tends to advect too much suspended sediment offshore, accounting for the small forecast gradients. The kriging and direct insertion assimilation schemes tend to reduce the bias by forcing the model to reset the gradients to more reasonable values, although longer times between updates bring the assimilation forecast values closer to the pure model values.

To further illustrate the forecast behavior along the coasts, Figure 5 also shows the model and assimilation forecasts near the coasts, along with data obtained by satellite and from EEGLE. The EEGLE data include both in situ samples and TSM measurements made by using a phytoplankton survey system (PSS). This system, described by Liebig et al. (2006), consists of a sensor package that changes depth as it is towed through the water at a relatively slow speed. The PSS thus provides a nearly continuous measure of the sampled variables through the water column for the length of the transect. The sensor package includes an optical particle counter that measures bulk light attenuation values. These are converted to TSM by using the method described by Winkleman et al. (1998). Figure 5 shows the pure model and assimilation forecasts for an hour within the PSS sampling period (St. Joseph and Muskegon transects) or the time period required to collect the grab samples (Chicago transect), the PSS data (St. Joseph and Muskegon), and the satellite data nearest in time to the other data. The satellite data are displayed both as values along the transect and as excerpts from the images that include the transects. In the case of the Chicago

transect, the nearest satellite data follow the water column observations by about three days. For the Muskegon transect, satellite images were available about three days on either side of the PSS data. Along the St. Joseph transect, the nearest satellite data precede the model forecasts and other observations by about 4 hours. The image collected at hour 522 was clear for all three transects. To illustrate the evolution of the nearshore features, we also show the hour 522 satellite data with the St. Joseph and Chicago transects.

The flatness of the pure model forecasts near the coasts is evident in all the transects shown in Figure 5. The assimilated forecasts are steeper, though they do not generally equal the gradients seen in the data. The satellite values agree well with the in situ samples and PSS values, though one has to view this agreement carefully, because both the PSS and satellite data were calibrated with data from the same set of in situ samples. The agreement between the satellite data and insertion forecast at St. Joseph reflects the fact that the satellite data were incorporated into the forecast at hour 379. In this particular, example the major differences between the insertion and model forecasts are seen in the region more than 10 km offshore. The TSM values estimated by the insertion forecast drop steeply and match the grab sample and PSS values, but the pure model forecast remains relatively constant, underestimating the observed gradient. A similar situation is seen in the Muskegon transect, where both the satellite data and PSS indicate a sharp drop-off in TSM beyond 10 km. Although the steep gradient is not so clear in the insertion forecast, we must consider that this forecast was last updated at hour 379, about three days before the PSS and grab sample collection and about five days before the next image. During that time, the insertion forecast will tend to move toward the pure model upon which it is based.

We had expected that kriging would improve upon direct insertion by smoothing the forecast fields in a way that captured the observed covariance of the observations. Our results, however, show that kriging reduces the forecast errors only minimally. One reason for this is that we assumed no measurement error so that the updated fields for direct insertion and kriging are identical at the cloud-free pixels. Also, as noted above, we used a very short correlation length scale ($\lambda = 2$) for kriging, which implies that only forecasts within a few pixels of cloud-free data are affected by the update step. Although we experimented with different covariance models, including ones that were locally anisotropic, none substantially improved the forecast results. This is a consequence of our assumption (Eq. 6) that the forecast errors are unbiased (i.e., have a mean value of zero). Thus, the kriging would tend to underpredict higher values in coastal regions, where cloud cover often obscures the images. We also found that using an error model that included a constant bias did not reduce the forecast error. Conceivably, one could construct a more complex model error function for use in an anisotropic and adaptive kriging procedure, but such an effort is beyond the scope of this paper.

One of the challenges associated with using satellite data is that the images are often incomplete and fragmented. Although our initial screening was intended to ensure that we began with fairly complete images, our results will be affected by discontinuities introduced by cloud boundaries and retrieval failures. Each of our assimilation methods produces a complete field at the update step. In the case of direct insertion, obscured or missing pixels are set to their last forecast value, which may be quite different from the value in a neighboring good pixel. Although kriging replaces the obscured pixel value with a weighted function of the nearby good observations, discontinuities in the updated fields are reduced only slightly, because the range parameter (λ) is small. Unfortunately, the prevailing southwesterly winds over southern Lake Michigan tend to result in formation of cumulus clouds over the eastern shoreline. Thus, this region, which also tends to have the highest variability in TSM, is more often obscured than other regions, and the errors in the gradient forecasts along the eastern shore are increased as a result.

The overall performance of the assimilation can be assessed by comparing time series of the forecasts obtained by using the pure model with those obtained by using direct insertion. Figure 6 shows these results for three near-shore stations around the southern basin. In addition to the forecast time series, we also have plotted the satellite data used in the assimilation, satellite data that were not used in the assimilation because the images from which they were extracted did not pass our screening, and data from the in situ sampling. The dotted portion of the black line shows the pure model forecast before any updating with satellite data. The assimilation forecasts diverge from the pure model forecasts after the first update at hour 282. Note that the assimilation forecasts are not nudged toward the observations but are obtained by running the model forward from the update time with only the initial conditions modified by the assimilated data. We see, for example, that at station J45 the assimilation at hour 379 requires the water column concentration to be reduced substantially. This relatively low concentration is confirmed by the grab sample collected at hour 376 and by the subsequent two satellite observations, the first of which was not included in the assimilation. After hour 522 the assimilation model forecasts a rapidly increasing sediment concentration, which again is confirmed by the satellite observation at hour 570. The pure model also forecasts an increase in concentration during this time period, but one of much lower magnitude. Finally, the pure model and assimilation forecast converge late in the record, after a prolonged period with little or no sediment resuspension.

The results shown in Figure 6 and Table 5 provide insight into both the importance of the various modeled processes and the values of the model parameters. Because we have not adjusted the model parameters, both the pure model and assimilation forecasts respond in the same ways to the forcing shear stress. The advective flows are also the same in both forecast schemes. Thus, differences between the two forecasts must result from differences

in the amount of available sediment and the suspended sediment concentration fields that are advected between pixels. The results in Table 5 show that advection is the single most important process for reducing the forecast error of the model. We already have noted the tendency of the model to transport too much material offshore. The difference in the forecast at Station J45, for example, occurs because the assimilation scheme keeps more material inshore and available for northward advection.

6 Summary and Conclusions

This paper reports a study of forecasting sediment concentrations in Lake Michigan by combining a 2-D sediment transport model with data obtained from a sequence of SeaWiFS satellite images. We considered a number of different forecasting methods, representing purely data-based approaches (climatology and persistence), a purely physical-model-based approach, and data assimilation approaches that combine the model and satellite data sequentially. To evaluate the methods, we determined the forecast errors for two different quantities: pixel-by-pixel log R_{RS} values and gradients. The data assimilation approaches improve forecasts by 20% over persistence approaches and by 40% over purely physical-model-based approaches.

We demonstrated that incorporating a time series of satellite images into a simple sediment transport model substantially improves forecasts of sediment concentrations in southern Lake Michigan. We see no reason why similar methods cannot be applied to other coastal regions where modeling and forecasting of sediment transport are of interest. Data availability need not necessarily be a limitation. Although we limited our original set of satellite images to reduce the effects of cloud contamination, we still had 20 good images spanning the 60-day study period, with an average of 5400 southern-basin pixels each, with which to work. This level of temporal and spatial data density would not be available from any other source.

A number of directions for future research remain. First, we would like to incorporate different sources of data into our assimilation scheme. As discussed earlier, we have available water samples and PSS measurements of TSM. We also have high-frequency time series of water currents available at 11 locations in the southern basin, and it would be natural to consider data assimilation schemes that combine these data with the hydrodynamic model. Presumably, this would result in improved advection fields, which could then be used to improve predictions of sediment concentrations. In a further step, the satellite, in situ, PSS, and current meter data could be used in a combined data assimilation scheme with a coupled hydrodynamic-sediment transport model. However, because the in situ measurements are sparse in space, careful construction of the kriging covariance model would be required.

Second, the methods used here could be extended to incorporate parameter estimation

for both the sediment transport model and the kriging covariance model. For example, the parameters could be chosen to minimize forecast RMSE or by using formal statistical methods such as maximum likelihood estimation. Third, it would be interesting to provide smoothed (retrospective) estimates of the sediment field over the modeling period. In contrast to the sequential methods described here, this would produce sediment fields without jumps at the observation times. These fields could be used as input to the biogeochemical models that have been developed for the lake. Finally, in addition to point forecasts, we would like to provide associated measures of uncertainty. The ensemble Kalman filter and its variants (Evensen, 1994; Tippett et al., 2003) provide a natural method for obtaining uncertainties, and their application for this purpose is the subject of our current research.

7 Acknowledgments

We thank the SeaWiFS Project and the Ocean Color Data Archive at the Goddard Space Flight Center for the production and distribution of the SeaWiFS data respectively. We also thank the EEGLE Project for collection and distribution of the in situ data used here. NOAA's Coastal Ocean Program supported supported work at ANL and GLERL, originally as part of EEGLE. Subsequent funding was provided by the United States Environmental Protection Agency (EPA) through Science To Achieve Results (STAR) Cooperative Agreement #R-82940201 to the University of Chicago for the Center for Integrating Statistical and Environmental Science (CISES). However, this research has not been subjected to the EPA's required peer and policy review and therefore does not necessarily reflect the views of the Agency, and no official endorsement should be inferred. This is GLERL Contribution Number XXXXX.

References

Baith, K., Lindsay, R., Fu, G., and McClain, C. (2001). SeaDAS, a data analysis system for ocean-color satellite sensors. *EOS Transactions of the American Geophysical Union* **82**, 202.

Behrenfeld, M., Randerson, J., McClain, C., Feldman, G., Loh, S., Tucker, C., Falkowski, P., Field, C., Frouin, R., Esais, W., Kolber, D., and Pollack, N. (2001). Biospheric primary production during an enso transition. *Science* **291**(5513), 2594–2597.

Beletsky, D. and Schwab, D. (2001). Modeling circulation and thermal structure in Lake Michigan: annual cycle and interannual variablility. *Journal of Geophysical Research* **106 (C9)**, 19745–19771.

Beletsky, D., Schwab, D., Roebber, P., McCormick, M., Miller, G., and Saylor, J. (2003). Modeling wind-driven circulation during the March 1998 sediment resuspension event in Lake Michigan. *Journal of Geophysical Research* **108**(C2), 20–1–20–13.

Binding, C., Bowers, D., and Mitchelson-Jacob, E. (2003). An algorithm for the retrieval of suspended sediment concentrations in the Irish Sea from SeaWiFS ocean colour satellite imagery. *International Journal of Remote Sensing* **24**, 3791–3806.

Binding, C., Bowers, D., and Mitchelson-Jacob, E. (2005). Estimating suspended sediment concentrations from ocean colour measurements in moderately turbid waters; the impact of variable particle scattering properties. *Remote Sensing of Environment* **94**(3), 373–383.

Brock, J. and McClain, C. (1992). Interannual variability in phytoplankton blooms observed in the northwestern Arabian Sea during the southwest monsoon. *Journal of Geophysical Research-Oceans* **97**(C1), 733–750.

Budd, J. and Warrington, D. (2004). Satellite-based sediment and chlorophyll a estimates for Lake Superior. *Journal of Great Lakes Research– Special Issue on Lake Superior* **30**(0), 459–466.

Chapra, S. C. (1977). Total phosphorus model for the Great Lakes. *J. Envir. Eng. Div., Amer. Soc. Civil Eng.* **103**(EE2), 147–161.

Chen, C., Wang, L., Ji, R., Budd, J., Schwab, D., Beletsky, D., Fahnenstiel, G., Vanderploeg, H., Eadie, B., and Cotner, J. (2004). Impacts of suspended sediment on the ecosystem in Lake Michigan: A comparison between the 1998 and 1999 plume events. *Journal of Geophysical Research-Oceans* **109**(C10).

Cressie, N. (1993). *Statistics for Spatial Data.* John Wiley and Sons, revised edition.

Eadie, B., Schwab, D., Johengen, T., Lavrentyev, P., Miller, G., Holland, R., Leshkevich, G., Lansing, M., Morehead, N., Robbins, J., Hawley, N., Edgington, D., and Hoof, P. V. (2002). Particle transport, nutrient cycling and algal community structure associated with a major winter-spring sediment resuspension event in southern Lake Michigan. *Journal of Great Lakes Research* **28**(3), 324–337.

Eadie, B., Schwab, D., Leshkevich, G., Johengen, T., Assel, R., Holland, R., Hawley, N., Lansing, M., Lavrentyev, P., Miller, G., Morehead, N., Robbins, J., and Hoof, P. V. (1996). Anatomy of a recurrent episodic event: a winter-spring plume southern Lake Michigan. *EOS, Transactions of the American Geophysical Union* **77**, 337–338.

Evensen, G. (1994). Sequential data assimilation with a nonlinear quasi-geostrophic model using Monte-Carlo methods to forecast error statistics. *Journal of Geophysical Research* **99**, 10143–10162.

Gaspari, G. and Cohn, S. (1999). Construction of correlation functions in two and three dimensions. *Quarterly Journal of the Royal Meteorological Society* **125**, 723–757.

Gerritsen, H., Boon, J., van der Kaaij, T., and Vos, R. (2001). Integrated modelling of suspended matter in the North Sea. *Estuarine, Coastal and Shelf Science* **53**, 581–594.

Gordon, H. and Wang, M. (1994). Retrieval of water-leaving radiance and aerosol optical thickness over the oceans with SeaWiFS: A preliminary algorithm. *Applied Optics* **33**, 443–452.

Hawley, N. and Lesht, B. (1992). Sediment resuspension in Lake St. Clair. *Limnology and Oceanography* **37**(8), 1720–1737.

Hughes, C., Jones, M., and Carnochan, S. (1998). Use of transient features to identify eastward currents in the Southern Ocean. *Journal of Geophysical Research-Oceans* **103**(C2), 2929–2943.

Kalnay, E. (2003). *Atmospheric modeling, data assimilation, and predictability.* Cambridge University Press.

Kostinoy, A., Ginzburg, A., Frankingoulle, M., and Delille, B. (2004). Fronts in the southern Indian Ocean as inferred from satellite sea surface temperature data. *Journal of Marine Systems* **45**(1-2), 55–73.

Krone, R. (1962). *Flume studies of the transport of sediment in estuarial shoaling processes.* Technical report, Hydraulic Engineering Laboratory and Sanitary Engineering Research Laboratory, University of California, Berkeley, California, U.S.A.

Lee, C.-H., Schwab, D., and Hawley, N. (2005). Sensitivity analysis of sediment resuspension parameters in coastal area of southern Lake Michigan. *Journal of Geophysical Research* **110**(C03004), 16.

Lesht, B. (1989). Climatology of sediment transport on Indiana Shoals, Lake Michigan. *Journal of Great Lakes Research* **15**, 486–497.

Lesht, B. and Hawley, N. (1987). Near-bottom currents and suspended sediment concentration in southeastern Lake Michigan. *Journal of Great Lakes Research* **13**, 375–386.

Lesht, B. M., Fontaine, T. D., and Dolan, D. M. (1991). Great-lakes total phosphorus model - post audit and regionalized sensitivity analysis. *Journal of Great Lakes Research* **17**(1), 3–17.

Lesht, B. M., Stroud, J. R., McCormick, M. J., Fahnenstiel, G., Stein, M. L., Welty, L. J., and Leshkevich, G. A. (2002). An event-driven phytoplankton bloom in southern Lake Michigan observed by satellite. *Geophysical Research Letters* **29**(8).

Liebig, J., Vanderploeg, H., and Ruberg, S. (2006). Factors affecting the performance of the optical particle counter in large lakes: Insights from Lake Michigan and laboratory studies. *Journal of Geophysical Research* **111**(C05502).

Mitchelson-Jacob, E. (1999). *Retrieval of Suspended Particulate Matter Concentrations from Ocean Colour Imagery.* Technical Report UCES Report U99-2, Document DP-CSM/1099-004, Unit for Coastal and Estuarine Studies, University of Wales, Bangor, Marine Science Laboratories, Menai Bridge, Anglesey LL59 5EY.

Mortimer, C. (1988). Discoveries and testable hypotheses arising from coastal zone color scanner imagery of southern Lake Michigan. *Limnology and Oceanography* **33**(2), 203–226.

Myint, S. W. and Walker, N. (2002). Quantification of surface suspended sediments along a river dominated coast with NOAA AVHRR and SeaWiFS measurements: Louisiana, USA. *International Journal of Remote Sensing* **23**(16), 3229–3249.

Ouillon, S., Douillet, P., and Andréfouët, S. (2004). Coupling satellite data with in situ measurements and numerical modeling to study fine suspended-sediment transport: a study for the lagoon of New Caledonia. *Coral Reefs* **23**, 109–122.

Partheniades, E. (1962). A study of erosion and deposition of cohesive soils in salt water. Ph.D. thesis, University of California, Berkeley.

Pleskachevsky, A., Gayer, G., Horstmann, J., and Rosenthal, W. (2005). Synergy of satellite remote sensing and numerical modeling for monitoring of suspended particulate matter. *Ocean Dynamics* **55**, 2–9.

Puls, W., Doerffer, R., and Sündermann, J. (1994). Numerical simulation and satellite observations of suspended matter in the North Sea. *IEEE Journal of Oceanic Engineering* **19**(1).

Ransibrahmanakul, V. and Stumpf, R. (2002). The use of AVHRR satellite data for estimating spatially varying critical wind stress in Florida Bay. *Journal of Coastal Research* **18**(2), 267–273.

Rao, Y., Murthy, C., McCormick, M., Miller, G., and Saylor, J. (2002). Observations of circulation and coastal exchange characteristics in southern Lake Michigan during 2000 winter season. *Geophysical Research Letters* **29**.

Schwab, D. and Bedford, K. (1994). Initial implementation of the Great Lakes Forecasting System: A real-time system for predicting lake circulation and thermal structure. *Water Pollution Research Journal of Canada* **29**, 203–220.

Schwab, D. and Beletsky, D. (2002). Hydrodynamic and sediment transport modeling of episodic resuspension events in Lake Michigan. In: M. Spaulding (ed.), *Proceedings of the Seventh International Conference on Estuarine and Coastal Modeling*, 266–279, St. Petersburg, FL.

Schwab, D., Beletsky, D., and Lou, J. (2000). The 1998 coastal turbidity plume in Lake Michigan. *Estuarine, Coastal and Shelf Science* **50**, 49–58.

Schwab, D., Bennett, J., Liu, P., and Donelan, M. (1984). Application of a simple numerical wave prediction model to Lake Erie. *Journal of Geophysical Research* **89**(C3), 3586–3589.

Stein, M. (1999). *Interpolation of Spatial Data: Some Theory for Kriging.* Springer.

Tippett, M., Anderson, J., Bishop, C., Hamill, T., and Whitaker, J. (2003). Ensemble square-root filters. *Monthly Weather Review* **131**, 1485–1490.

Uddstrom, M. and Oien, N. (1999). On the use of high-resolution satellite data to describe the spatial and temporal variability of sea surface temperatures in the New Zealand region. *Journal of Geophysical Research-Oceans* **104**(C9), 20729–20751.

Warrick, J., Mertes, L., Siegel, D., and Mackenzie, C. (2004). Estimating suspended sediment concentrations in turbid coastal waters of the Santa Barbara Channel with SeaWiFS. *International Journal of Remote Sensing* **25**(10), 1995–2002.

Winkleman, A., Stabenau, E., and Eadie, B. (1998). *Particle distribution and concentration of total suspended matter in southern Lake Michigan.* NOAA Technical Memo ERL GLERL-105, Great Lakes Environmental Research Laboratory, Ann Arbor, MI, 48105.

Appendix: Preconditioned Conjugate Gradient for Kriging

The kriging formula Eq. (8) can be rewritten as

$$\mathbf{y}^u = \mathbf{y}^f + \mathbf{\Sigma H' Q}^{-1}\mathbf{e},$$

where $\mathbf{e}$ is the $m \times 1$ forecast error, and $\mathbf{Q} = \mathbf{H\Sigma H'}$ is the $m \times m$ forecast covariance matrix at the observed locations. The calculation is carried out in three steps: (1) Solve $\mathbf{Qz} = \mathbf{e}$. (2) Compute $\mathbf{w} = \mathbf{\Sigma H'z}$. (3) Compute $\mathbf{y}^u = \mathbf{y}^f + \mathbf{w}$. The last two steps are straightforward: Step 2 involves a sparse matrix-vector multiplication, and Step 3 requires vector addition. Step 1 is more involved, as it requires solving a large system of order m. We propose a variational method to solve the system, in which we define the function

$$f(\mathbf{z}) = \frac{1}{2}\mathbf{z'Qz} - \mathbf{z'e},$$

and let $\mathbf{z}$ be the minimizer of $f(\cdot)$. A preconditioned conjugate gradient (CG) algorithm is used to perform the minimization. In the CG method, we use circulant embedding to compute matrix-vector products efficiently via the fast Fourier transform. The computational complexity for each CG iteration is $O(\tilde{n}\log_2\tilde{n})$, where $\tilde{n} \geq 2n_1n_2$ is the order of the circulant matrix, and $n_1 = 131$ and $n_2 = 251$ are the dimensions of the modeling grid in our application.

Table 1: Summary of satellite log remote sensing reflectance (log R_{RS}) values for all 20 images used in the forecast study.

March 1998 Images						April 1998 Images					
Date	Hour	m	Mean	Min	Max	Date	Hour	m	Mean	Min	Max
3/12	282	5398	-3.40	-4.28	-1.77	4/4	834	7092	-3.72	-4.53	-1.95
3/12	283	5491	-3.36	-3.97	-1.55	4/5	859	6601	-3.68	-4.45	-1.99
3/16	379	4580	-3.32	-3.97	-1.95	4/11	1003	3685	-3.54	-4.41	-1.94
3/21	498	5414	-3.53	-4.15	-1.89	4/12	1026	6548	-3.54	-4.33	-1.87
3/22	522	6600	-3.49	-4.22	-1.91	4/17	1146	6587	-3.72	-5.48	-1.89
3/23	546	5646	-3.45	-4.48	-1.88	4/18	1171	3563	-3.71	-5.07	-1.97
3/23	547	6291	-3.43	-4.63	-1.89	4/19	1194	3905	-3.61	-4.60	-1.89
3/24	570	7079	-3.52	-4.53	-1.92	4/23	1290	6800	-3.80	-4.54	-2.02
3/26	618	4176	-3.31	-4.22	-1.80	4/27	1387	3929	-3.88	-4.31	-2.16
3/29	691	4146	-3.33	-3.92	-1.91	4/28	1410	4633	-3.80	-4.60	-2.00
Total:		54821	-3.43	-4.63	-1.55	Total:		53343	-3.70	-5.48	-1.87

Table 2: Summary of near-surface total suspended material (TSM) measurements during March-April, 1998.

Date	Hour	Stat	TSM	Date	Hour	Stat	TSM
3/16	373	J10	32.87	4/10	976	M45	1.90
3/16	379	J73	1.29	4/24	1310	R10	6.19
3/16	383	J45	1.84	4/24	1318	DWS	0.89
3/16	383	J30	13.04	4/25	1323	A4	2.31
3/17	398	G30	1.52	4/25	1341	J40	1.22
3/17	400	G10	34.21	4/25	1343	J20	4.54
3/18	424	C10	11.55	4/26	1344	J10	4.29
3/18	425	C30	0.99	4/27	1382	A3	10.24
3/18	427	C45	2.83	4/27	1384	G10	10.51
3/19	450	M110	1.16	4/27	1387	G20	1.92
3/19	453	M45	4.89	4/27	1391	A2	7.76
4/5	840	J30	4.00	4/28	1395	A1	26.42
4/6	888	M110	1.10	4/28	1398	R10	15.60

Table 3: Initial conditions and parameter values for the sediment transport model.

Parameter	Symbol	Value
Initial bed	b_0	1 mm
Initial TSM	c_0	0.01 mg/L
Settling rate	w_s	2.5×10^5 m/s
Resuspension rate	ϵ	100 kg/m^2/s
Critical shear stress	τ_c	0.30 N/m^2

Table 4: Summary of the one-image-ahead forecast bias and root mean squared error (RMSE) for satellite log R_{RS}, R_{RS} and TSM, and for in situ data. The bottom row shows the mean and standard deviation for the observed data.

	Satellite Data						*In Situ*	
	log R_{RS}		R_{RS} (%)		TSM		TSM	
Method	Bias	RMSE	Bias	RMSE	Bias	RMSE	Bias	RMSE
Climatology	0.346	0.489	1.10	1.97	1.08	2.85	4.75	9.73
Pure model	0.092	0.413	0.30	1.63	0.45	2.54	3.19	8.50
Persistence	-0.022	0.299	-0.07	1.37	-0.07	2.43	1.74	9.07
DA-insertion	-0.025	0.238	-0.03	1.03	0.09	1.85	2.26	7.35
DA-kriging	-0.036	0.237	-0.06	1.01	0.05	1.79	1.93	6.90
Observed	-3.570	0.496	3.28	2.30	2.11	3.31	7.89	9.60

Table 5: Summary of the one-image-ahead log R_{RS} forecast bias and RMSE for the direct insertion approach with different combinations of the sediment model components (advection, settling, and resuspension).

Model Components	Bias	RMSE
Null	-0.022	0.299
Settling	0.040	0.348
Resupension	-0.032	0.294
Settling, Resuspension	-0.003	0.286
Advection	-0.038	0.277
Advection, Settling	0.018	0.282
Advection, Resuspension	-0.057	0.254
Advection, Settling, Resuspension	-0.025	0.238

Table 6: Summary of the one-image-ahead forecast bias and RMSE for the east-west gradient of log R_{RS}. The bottom row shows the mean and standard deviation for the observed gradients.

	West		Offshore		East	
Method	Bias	RMSE	Bias	RMSE	Bias	RMSE
Climatology	-0.008	0.186	0.009	0.089	0.027	0.225
Pure model	-0.075	0.222	0.003	0.103	0.043	0.231
Persistence	0.000	0.271	0.001	0.131	0.016	0.307
DA-insertion	-0.023	0.214	0.001	0.095	0.002	0.216
DA-kriging	-0.019	0.211	0.001	0.090	0.002	0.214
Observed	-0.104	0.217	0.012	0.088	0.068	0.232

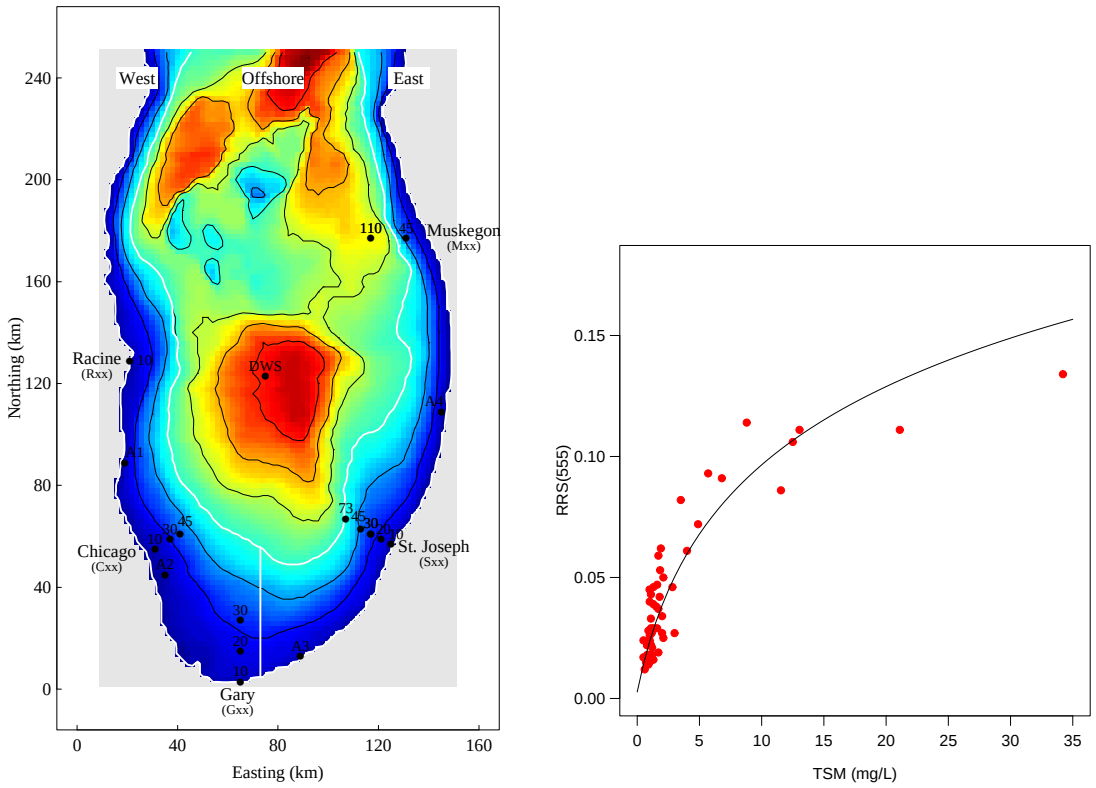

Figure 1: Southern Lake Michigan water depths and in situ data. Left panel: Bathymetry of southern Lake Michigan (where blue is shallower water, and red is deeper water), three spatial regions, and locations of the 1998-1999 in situ measurements. Right panel: 62 matched sediment and reflectance measurements and fitted with R_{RS}-TSM function.

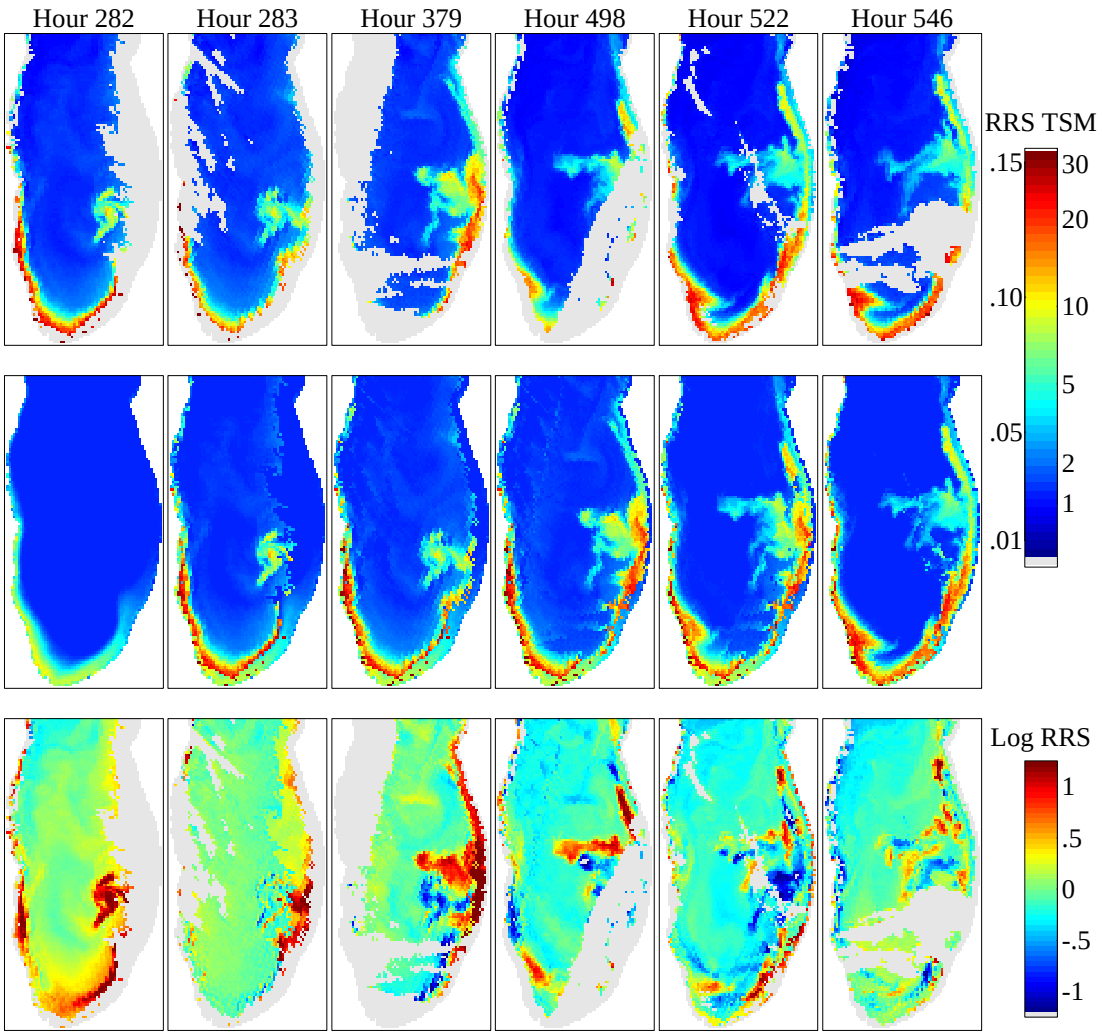

Figure 2: Results for the persistence forecasts at the first six image times. Top row: satellite data; middle row: persistence forecast; bottom row: forecast error (data minus forecast). Gray pixels indicate cloud-covered regions.

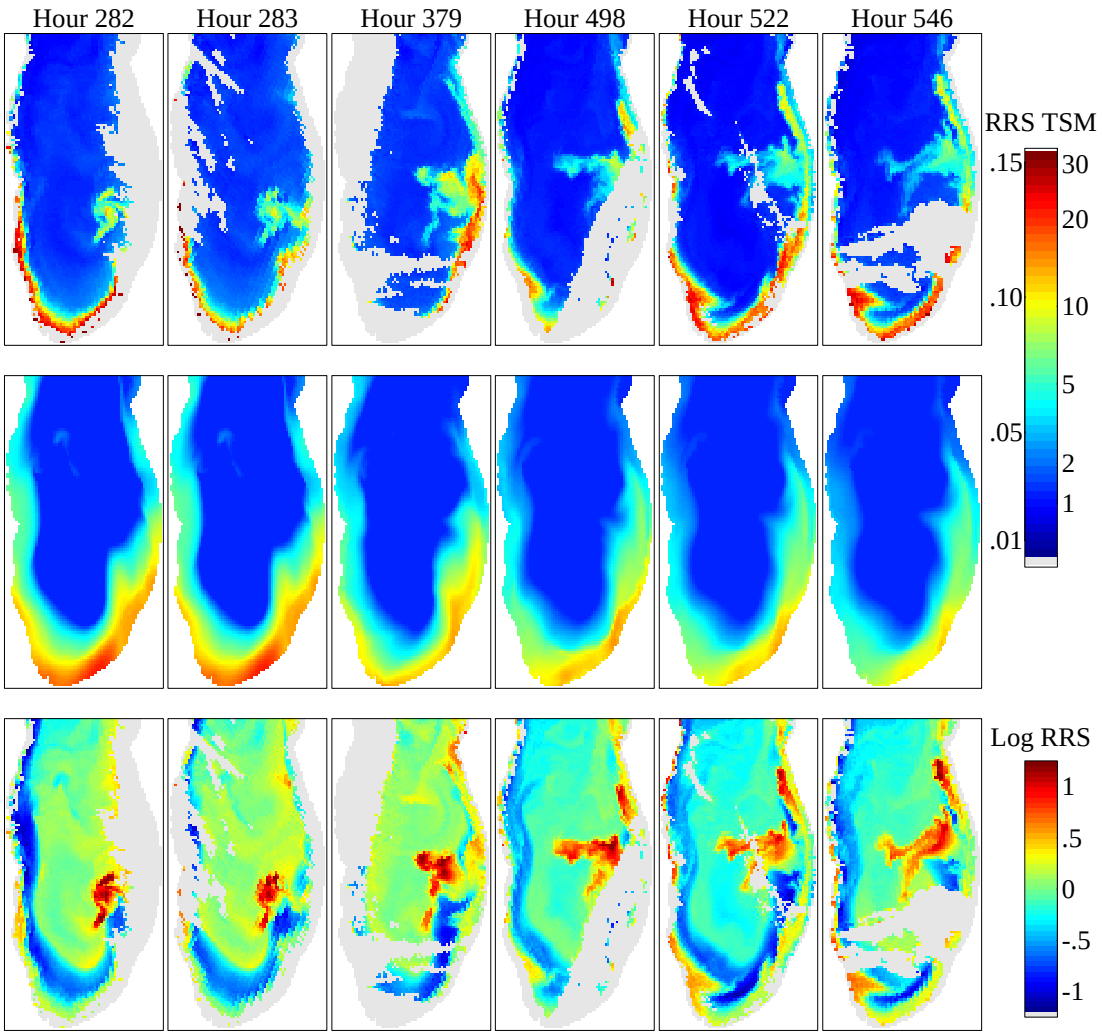

Figure 3: Results for the pure model forecasts at the first six image times. Top row: satellite data; middle row: pure model forecast; bottom row: forecast error (data minus forecast). Gray pixels indicate cloud-covered regions.

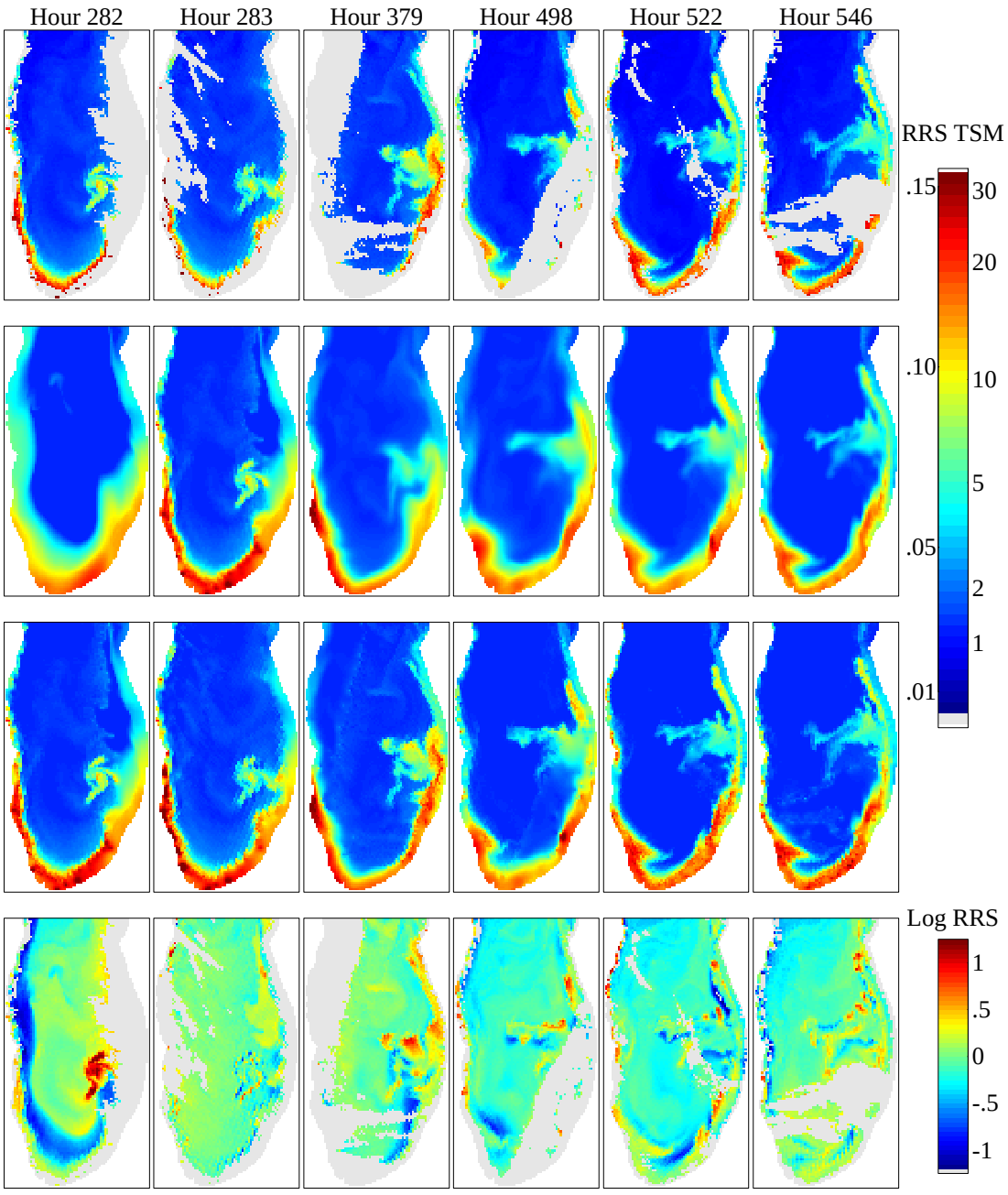

Figure 4: Results for the kriging forecasts at the first six image times. Top row: satellite data; second row: forecast; third row: updated field; bottom row: forecast error (data minus forecast). Gray pixels indicate cloud-covered regions.

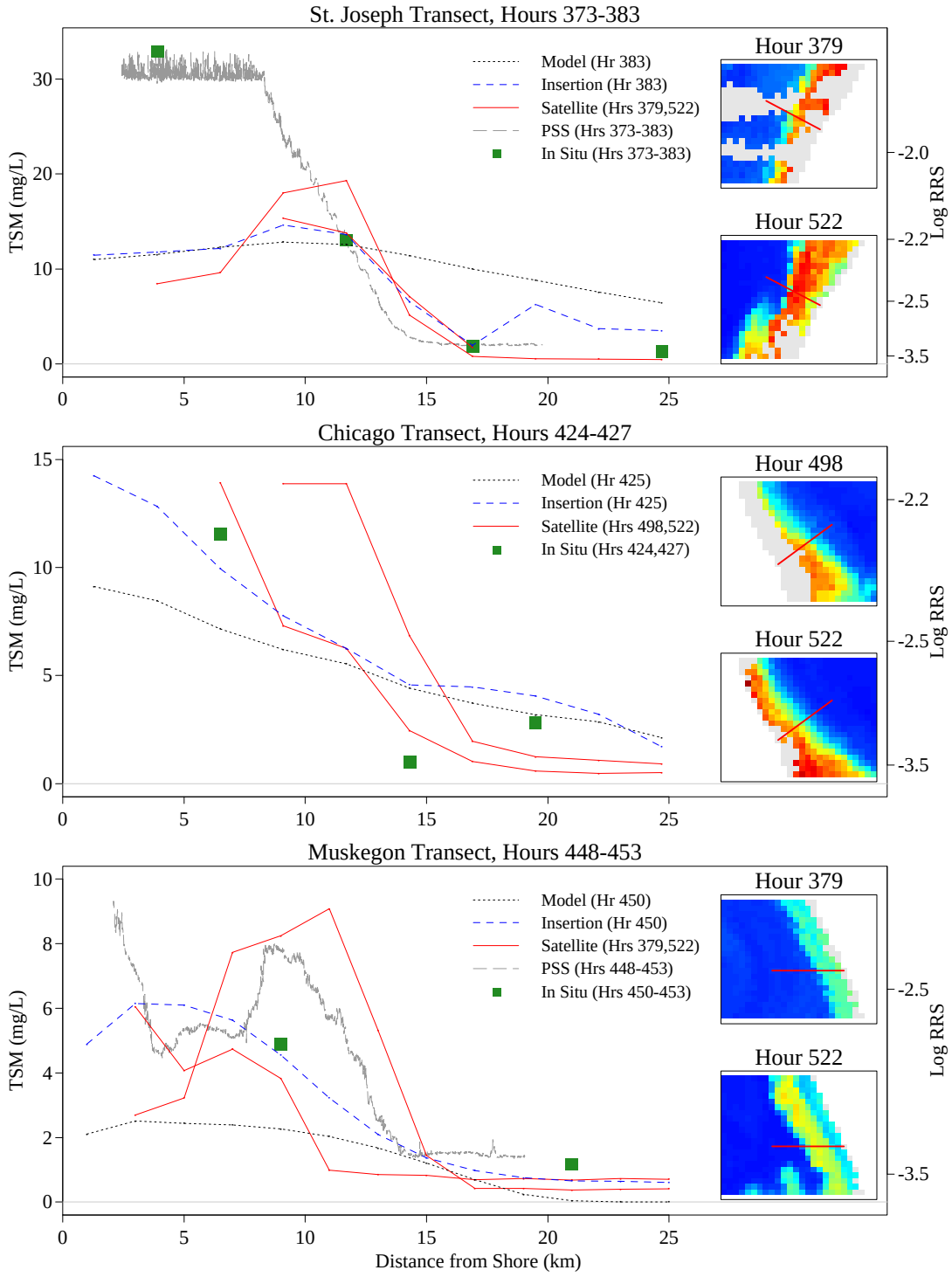

Figure 5: Forecasting results for the pure model and direct insertion methods along three transects. Satellite, in situ, and phytoplankton survey system (PSS) data during the same time period are also plotted. The inset images show the satellite data at the nearest two cloud-free image times, and the transects are indicated by red line segments.

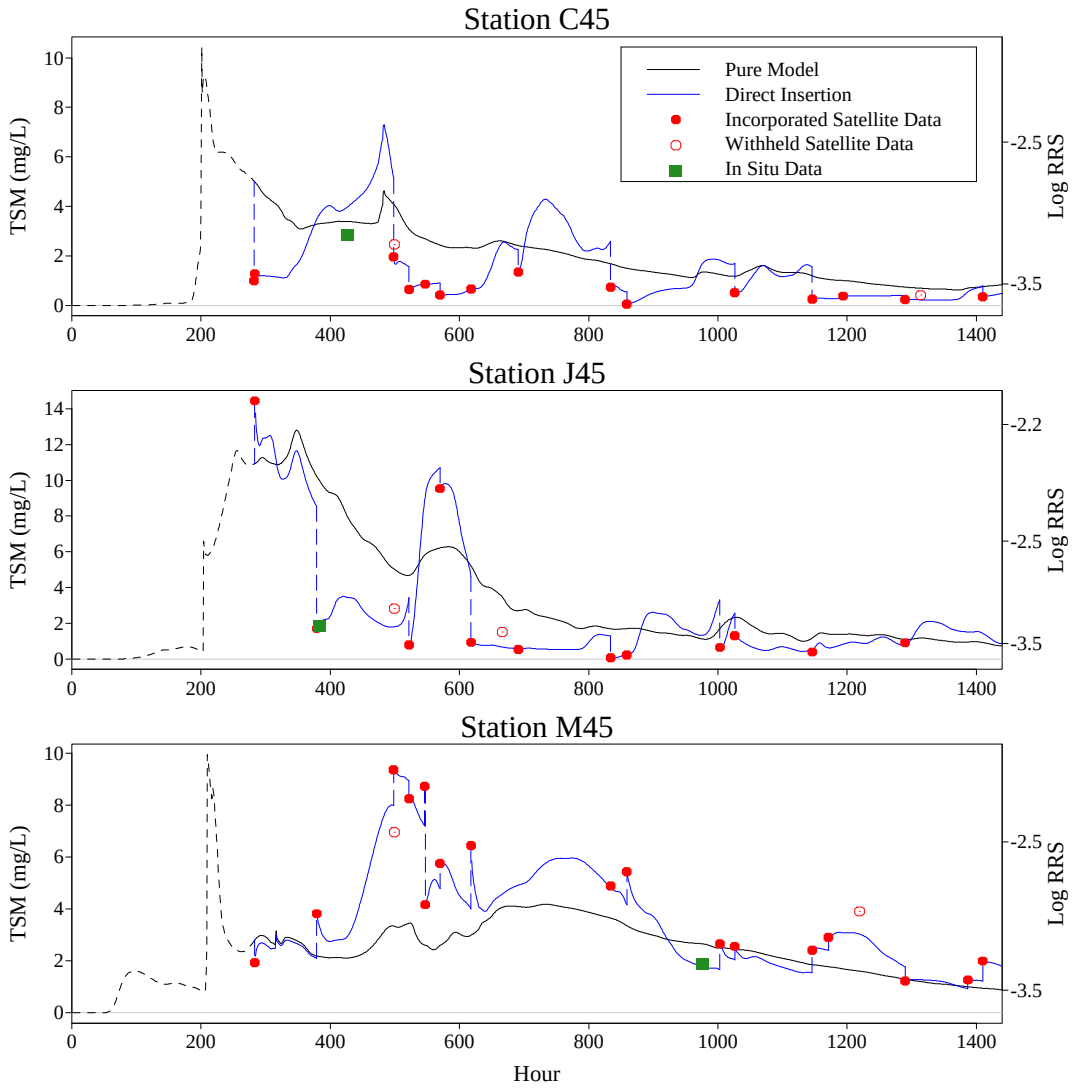

Figure 6: Time series of the pure model and direct insertion forecasts, along with satellite and in situ data at three monitoring stations (see Fig. 1). The black solid line is the pure model forecast; the blue solid line is the direct insertion forecast; the black dashed line is the forecast for both methods, which are identical until the first assimilation time (hour 282); and the blue dashed line is the shift from the forecast to the update value for the direct insertion approach. The closed circles (satellite data) were used in the assimilation, while the open circles (satellite data) and squares (in situ data) were not.